Pulsations and flows in tissues: two collective dynamics with simple cellular rules

Raghavan Thiagarajan,[1,2,3,4] Alka Bhat,[1,2,3,4] Guillaume Salbreux,[5] Mandar M. Inamdar,[6,*] and Daniel Riveline[1,2,3,4,†]

[1] *Institut de Génétique et de Biologie Moléculaire et Cellulaire, Illkirch, France*

[2] *Laboratory of Cell Physics ISIS/IGBMC, CNRS and Université de Strasbourg, Strasbourg, France*

[3] *Centre National de la Recherche Scientifique, UMR7104, Illkirch, France*

[4] *Institut National de la Santé et de la Recherche Médicale, U964, Illkirch, France*

[5] *The Francis Crick Institute, 1 Midland Road, London NW1 1AT, United Kingdom*

[6] *Department of Civil Engineering, Indian Institute of Technology Bombay, Mumbai 400076, INDIA*

(Dated: October 4, 2021)

Collective motions of epithelial cells *in vivo* are essential for morphogenesis in developmental biology. Tissues elongate, contract, flow, and oscillate, sculpting embryos. These tissue level dynamics are known, but their physical mechanisms at the cellular level are unclear, with various behaviors that depend on the tissues and species. Moreover, investigations on *in vitro* tissue behavior usually focus on only one type of cell dynamics and use diverse theoretical approaches, making systematic comparisons between studies challenging. Here, we show that the very same epithelial monolayer of Madine Darby Canine Kidney (MDCK) cells can exhibit two types of tissue kinematics, pulsations, and coherent flows. We also report that these distinct motions can be controlled with internal and external cues by using quantitative live imaging of the acto-myosin cytoskeleton, specific inhibitors, microfabrication, and friction modulation of the substrate. We further demonstrate with a unified vertex model that both behaviors depend on the interplay between velocity alignment and random diffusion of cell polarization. When alignment and diffusion are comparable, a pulsatile flow emerges, whereas the tissue undergoes long-range flows when velocity alignment dominates. We propose that environmental friction, acto-myosin distributions, and cell polarization kinetics serve as the essential factors regulating the dynamics of tissue morphogenesis.

* minamdar@iitb.ac.in

† riveline@unistra.fr

I. Introduction

During development, tissue dynamics shapes organs with remarkable correlations in space and time [1–5]. Groups of hundreds/thousands of cells flow like liquids in developing embryos in *Drosophila* [6], zebrafish [7], and insects [8]. Solid-like pulsatile movements are also reported in *Caenorhabditis elegans* [9]; in the developing heart of zebrafish, where collective oscillatory motion is required for its proper development; and, more generally, in muscle layers spanning epithelial layers [10]. These millimeter-scale changes in shapes involve the acto-myosin cytoskeleton, which drives tissue movement and generates stress at the organism level [1, 3, 11]. These motions and deformations drive the shaping of tissues, eventually setting organ functions through cell differentiation. Altogether, flows and pulsations are general phenomena in morphogenesis.

Strikingly, these changes in shapes occur in various species with conserved 'families' of tissue transformation, such as elongation and gastrulation, among many morphogenetic events. Even if their genetic backgrounds are different, the basic common mechanisms at the cellular level are expected to be shared among different biological model systems [12]. Indeed, simple physical rules to achieve morphogenesis are known: (i) tissues are composed of cells that change their shapes over time, (ii) cells in tissues interact with their neighbors by adhering to each other via adherens junctions and to the surrounding extra-cellular matrix through focal contacts [13]. It is puzzling that the same monolayer of cells connected to each other and the matrix can undergo distinct dynamics. With their complete identifications, these cellular interactions are expected to lead to self-organization at the tissue level. Moreover, simple changes in these basic rules can lead to very different tissue-level shape transformations reported *in vivo* [14]. However, these changes at the cellular level are yet to be identified through experiments with epithelial cells exhibiting various morphogenetic transformations in controlled conditions.

Various biological systems share a number of dynamical morphogenetic events *in vivo*, but they are rarely investigated with a unified physical model to observe their diversity. For instance, during blood vessel formation, seven events were reported to contribute to angiogenesis, i.e., cell migration, anastomosis, apical membrane fusion, cell elongation and rearrangements, cell splitting, cell self-fusion, and cell division [15, 16]. Each of them may contribute to the formation of the vessel and the associated cellular flows. More generally, this so-called mechanism of 'branch formation' is essential to shape organs, and goes beyond the formation of the vascular systems [17, 18]. In

fact, during branch formation, the lungs, kidneys, and mammary glands undergo these different dynamic events at the single cell level, leading to global cellular reorganizations. Cells at the 'tip' of the branches are mesenchymal (behaving as migrating single cells) and they are connected to the 'stalk' made of epithelial cells (behaving as a connected tissue), which may undergo passive motion and/or rearrangements through neighbor exchanges and cell proliferation for tracheal branching and vertebrate angiogenesis [17, 18]. However, the identification of conserved principles still lacks a proper understanding of physical rules for cells interactions that lead to global movements.

Several types of single-cell dynamics in morphogenesis, such as the growth of protrusions through filopodia and lamellipodia, binding to the surrounding extracellular matrix with focal contacts, and connecting with the neighboring cells through adherens junctions, have been reported in these examples in morphogenesis [19]. Cells can also have motility either as independent individuals or collectively in a group. In the latter case, it is often difficult to disentangle the motion of cells as arising from, for example, either active single-cell motion or from cell proliferation due to an increase in cell density and the associated reorganization of tissues with gradients in cell density stress [20]. Thus, in the search for quantitative methods to characterize collective motions beyond experiments with live microscopy, new approaches from theoretical physics for active matter are needed [21]. Indeed, tight and quantitative comparisons with numerical simulations are known to be efficient in testing these collective dynamics of groups of cells emerging out of rules of interactions at the cellular levels.

Another level of complexity is related to the cell state, which may change during development, for example, through differentiation and mesenchymal-to-epithelial transitions [22]. Changes in cell states can be either chemical or mechanical or both during the subsequent steps following exit from stemness state. Biological changes in cells are also accompanied by mechanical modifications and alterations in contractility and intercellular adhesion due to changes in proteins expressions and their levels [22, 23]. However, if the chemical state alters the mechanical state of the cells at any time, physical principles governing these morphogenetic events are robust and still at play irrespective of the cell states. Thus, the search for simple mechanisms is essential to decipher the rules of tissue morphogenesis during development. Specifically, even in these *in vivo* situations, groups of cells move as a whole, and, since long ago, the existence of cellular flows and pulsations is recognized in developmental biology across model systems. Hence, unifying experiments tightly

coupled to models are expected to unravel new schemes of cell self-organization.

With this aim, we followed the dynamics of epithelial Madine Darby Canine Kidney (MDCK) monolayer *in vitro* on flat 2D surfaces as a paradigm for morphogenesis in general [24–27]. We focused on two dynamics of collective cell movements, pulsations and flows, which as per our observation co-existed in standard 2D cell culture *in vitro*. We reasoned that the experimental control of each type of motion would guide us in understanding their cellular origins and successfully tested this assumption. First, we generated pulsations by modifying the friction between the tissue with surfaces patterned with fibronectin at the spontaneous coherence length scale of the monolayer. We then induced cellular flows by exposing the monolayer to cytoskeletal drugs. We also generated pulsations in conditions of flows by using laser ablation. To shed light on the underlying cellular mechanisms, we performed numerical simulations based on a unified vertex model with cell motility and successfully reproduced both types of motion by modulating just two factors.

II. Characterizing the spontaneous flow in epithelial monolayers

We seeded MDCK cells on glass substrate and acquired time-lapse images after the monolayer reached confluency. As noted previously [25, 26], confluent monolayers of MDCK underwent complex flow patterns that changed rapidly over time and eventually slowed down because of cell proliferation. To quantify the spatio-temporal patterns of cellular movements, we acquired the time-dependent velocity field using particle inference velocimetry (PIV) on the time-lapse images (Figs. 1a and 1d and Supp. Fig. 3). The MDCK monolayer seemed to exhibit temporally periodic patterns of spatially contractile and expanding cellular movements. To quantify local area changes in the tissue due to these pulsatory patterns, we used the velocity field to calculate the flow divergence (see Materials and Methods and Supplementary Information Sections IA and IB for details). The divergence and velocity fields showed that the flow field was correlated in space on a characteristic length scale of $\approx 200\ \mu$m (Figs. 1c and 1f). Focusing on the domains of this size (Figs. 1a and 1d), we noticed regions with visible pulses of contracting and expanding tissues (Figs. 1a-c and Movie 1) for approximately 5 h, or areas where the flow appeared to be more uniform and correlated over a larger length scale (Figs. 1d-f and Movie 2). In the pulsatile regions, we generally observed +1 topological defects in the velocity field (Fig. 1a, second row and Supplementary Information Section IC) and typically saw $2-4$ pronounced pulses in the velocity divergence (see Fig. 1b and the autocorrelation plot in the inset).

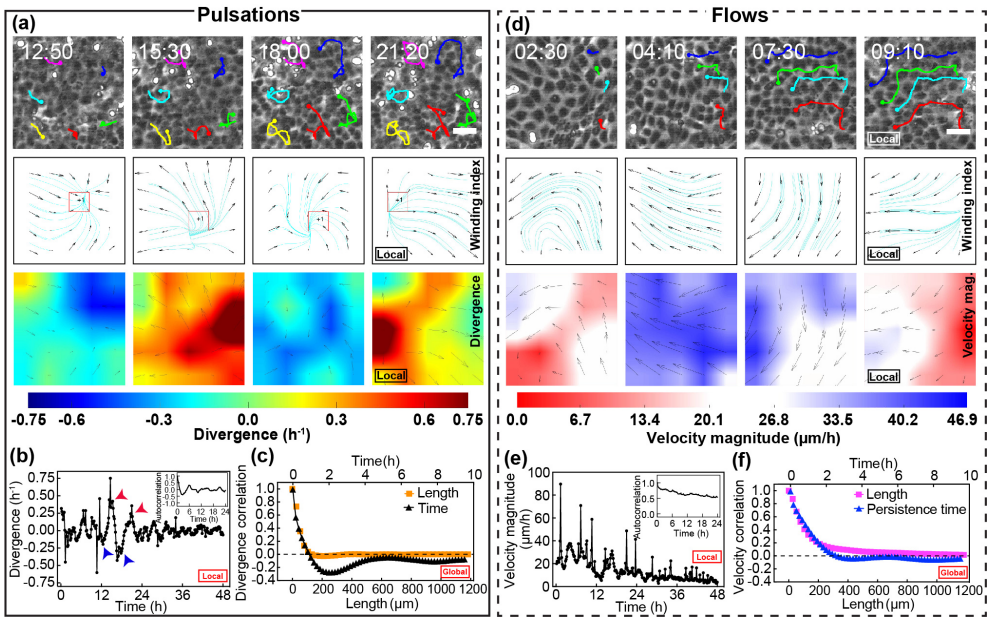

Figure 1. Spontaneous pulsations and flows in an epithelial monolayer. (a), (b), (d), and (e) represent the local characteristics of the monolayer. (a) shows snapshots of the contraction and expansion phases of one period of a pulsating domain, and (d) shows snapshots of a flow domain. In (a) and (d): the first row corresponds to phase-contrast images, and tracking highlights the back-and-forth movement of cells during pulsation in (a) and flow trajectory in (d); the second row shows the winding number analysis for the snapshots in the first row, and the third row shows the corresponding divergence and velocity magnitude plots, respectively, for (a) and (d). Scale bar 50 μm. Time is in hh:mm. In those panels indicating the nature of the divergence field, blue indicates contraction, and red indicates expansion; similarly, in those panels indicating velocity magnitude, red and blue indicate low and high velocities, respectively. The numerical values are specified in the corresponding color bars. (b) The mean divergence plot for the pulsatile domain over 48 h represented in (a) and in Movie 1. (e) The mean velocity magnitude plot of the flow domain shown in (d) and in Movie 2. Arrows in (b) indicate the data points corresponding to snapshots in (a). Insets in (b) and (e) show the autocorrelation of divergence (b) and velocity magnitude (e). (c) and (f) represent the global characteristics of the monolayer and show the divergence and velocity correlations, respectively, for distance and time for the same experiment over 48 h.

To quantify the tissue kinematic behavior over wider length scales, we calculated correlation functions in space and time for the velocity field and its divergence for the entire region under experimental consideration (Figs. 1f and 1c, respectively, and Supp. Fig. 3). We determined the correlation function of the divergence at the same spatial but different time points, $\langle \mathrm{div}(\mathbf{x},t)\mathrm{div}(\mathbf{x},t+\tau)\rangle_{\mathbf{x},t}$,

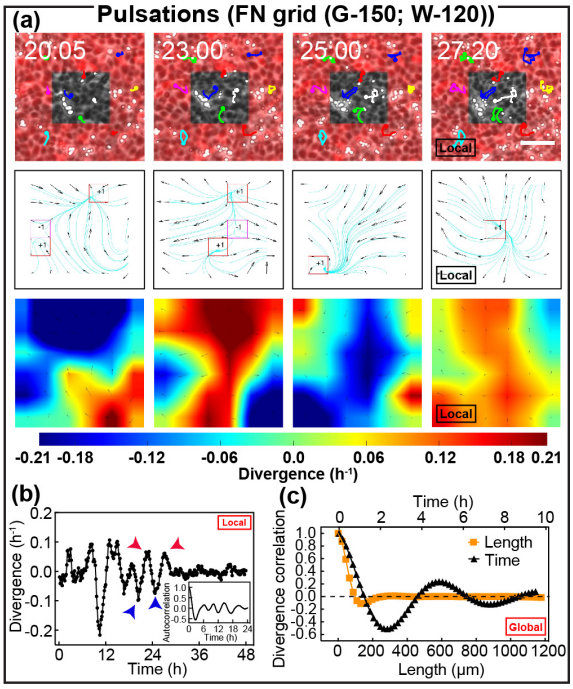

Figure 2. Substrate friction determines the intrinsic length scale of pulsations. (a)-(b) represent the local characteristics, and (c) illustrates the global characteristics. (a) shows a typical sub-unit of the fibronectin (FN) grid shown in Supp. Fig. 2. Here, the first row shows snapshots of one contraction expansion cycle of a pulsatile domain in a single grid unit where tracking highlights the cell trajectories during pulsations. Similarly, the second and third rows show the topological defects and divergence, respectively, for the snapshots in the first row. Color bar indicates the scale for divergence maps where blue and red indicate contraction and expansion, respectively. Scale bar, 100 μm and time in hh:mm. (b) shows the mean divergence plot that highlights the variations in divergence over 48 h for the FN grid domain in (a) and in Movie 4. Arrows indicate data points corresponding to the snapshots in (a), and the inset shows the autocorrelation. (c) The time correlation function for the corresponding divergence field exhibits striking oscillatory behavior with a period of approximately 5 h. The divergence correlation function in space also shows a minimum at approximately 150 μm, which reflects the periodic pulsatory pattern in space.

as a function of time-interval τ. It exhibited oscillatory behavior with a period of about 5 h, indicative of periodic pulsatile movements occurring in the tissue. By calculating the spatial correlation function, $\langle \mathrm{div}(\mathbf{x}+\Delta\mathbf{x},t)\mathrm{div}(\mathbf{x},t)\rangle_{\mathbf{x},t}$, as function of $r = |\Delta\mathbf{x}|$, we found that the divergence was also correlated in space on a length scale of approximately 200 μm (Fig. 1c), which corresponds to approximately 15 cell lengths (see Section VIII Materials and Methods and Supplementary Information). Similarly, we noted a spatial decay in the velocity correlation function of $\approx$ 200 μm

that is consistent with the characteristic correlation length for divergence (Fig. 1f). The velocity field exhibited a temporal decay of a few hours, and is larger than the correlation time of the divergence. This finding is consistent with our observation of regions moving coherently with a relatively uniform velocity on long time scales (Fig. 1d). Taken together, divergence and velocity correlation plots highlight different collective features of cell motion in the monolayer.

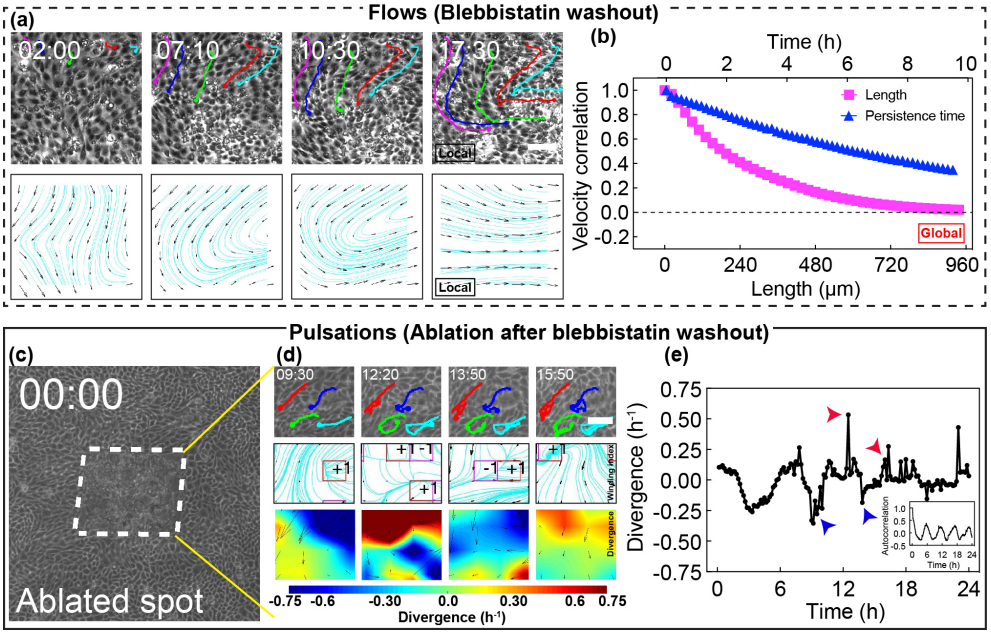

Figure 3. The transition from pulsations to flows and back to pulsations. (a)-(b) Resetting myosin activity (incubation with blebbistatin for 12 h and wash-out) leads to the transition from pulsations to flows. (a) and (b) highlight the local and global flow characteristics, respectively. The first row of (a) shows snapshots of phase-contrast images where the tracking highlights flow behavior. The second-row shows streamlines without the presence of topological defects. Scale bar, 100 μm. See also the associated Movie 7. (b) shows the spatial and temporal correlation plots for velocity magnitude over 36 h. (c)-(e) Ablation of tissue performed after flows that resulted from resetting myosin activity leads to pulsatile behavior. (c) shows snapshot of phase contrast image with the ablated spot highlighted by dotted lines. Scale bar, 100 μm. Time is in hh:mm. See the associated Movie 9 and Supp. Fig. 6d corresponds to the ablated region in (c). The first row of (d) shows snapshots of phase-contrast images where the tracking highlights back-and-forth pulsatile movements. The second and third rows show winding number and divergence respectively. Scale bar, 50 μm. Time is in hh:mm; (e) shows the mean divergence plot over 24 h for the pulsatile domain shown in (d). Arrows indicate the data points corresponding to snapshots in (d), and the inset shows the autocorrelation.

III. Pulsatile flows can be modulated by spatially periodic tissue-substrate interaction

We next sought to test whether the period and magnitude of pulsatile flows could be influenced experimentally. Considering the cell monolayer as a layer of active material interacting with the underlying substrate, we reasoned that modulating the tissue-substrate interaction in a spatially periodic fashion would allow to influence the tissue-scale collective flow. For this purpose, by using micro-contact printing (see Section VIII Materials and Methods), we deposited the extracellular matrix protein fibronectin as square motifs of controlled dimensions, called $G-75$ μm, $G-150$ μm, $G-300$ μm (see Fig. 2a, Supp. Fig. 4, Supp. Figs. 5a and 5d, and Movies 3-5). We kept the width of the fibronectin regions $W = 120$ μm to be the same for all three cases while varying the size G of the central region. We reasoned that fibronectin coating would locally increase the friction between the tissue and its substrate and separate the entire tissue region into areas of high and low friction (Supp. Fig. 4). We chose the dimension of these patches $G + W$ to be around the size of the domains of spontaneous cell pulsations.

We then quantified the temporal and spatial correlation of the flow divergence for the entire region. As in the control case, here also we observed the presence of oscillations with period of around 5 h (Supp. Fig. 4, Fig. 2c, and Supp. Figs. 5c and 5f). Remarkably, correlation plots of divergence indicated that the oscillatory component of the flow, as quantified by the dampening of the oscillation in the temporal correlation of the divergence, was maximal when the size of the motifs matched the spontaneous extension of pulsations, in the $G - 150$ μm case (Fig. 2, Movie 4). In contrast, when the grid-size was smaller ($G - 75$ μm, Supp. Figs. 5a-c, and Movie 3) or larger ($G - 300$ μm, Supp. Figs. 5d-f, and Movie 5), pulsations were less pronounced. It is worth noting that the magnitude of divergence of tissue flow was increased in the larger grids case (Fig. 2b, Supp. Fig. 5e) compared with that in smaller grids (Supp. Fig. 5b). This observation is consistent with the notion of lower overall friction between the tissue and its substrate when the fraction of substrate area covered by fibronectin is lower.

In these different conditions, more than $\approx 50\%$ of the grids exhibited sustained oscillations. Oscillations lasted for ≈ 48 h, corresponding to a couple of cycles in the $G - 75$ μm case, six cycles in the $G-150$ μm case, and a couple of cycles in the $G-300$ μm case. Decay in oscillation amplitude was possibly associated with cell proliferation leading to reduced tissue motion over time. We also noticed that the number of ± 1 defects was larger in the $G-75$ μm and $G-300$ μm cases than in the

$G-150$ μm case (Figs. 2a, Supp. Figs. 5a and 5d). Finally, in the 'resonant' case of $G-150$ μm, we aimed to decrease friction in the central, non-adhesive region of the pattern through incubation with poly(l-lysine) grafted with poly(ethylene glycol) (PLL-g-PEG), which passivates the surface. This process led to 'agitated' pulsations, involving localized rapid motions of cells within the passivated square, and this further supports the role of friction in the process (Movie 6). These results support the notion that friction can influence the nature of cellular movements. Taken together, these results show that the magnitude of pulsatile flow can be controlled by spatially modulating tissue-substrate interaction.

IV. Generation of long-range flows in epithelial monolayers

We then examined whether the correlation length of the flow could be experimentally modified. Interestingly, we found that incubation for 12 h with cytoskeleton inhibitors, followed by washing,

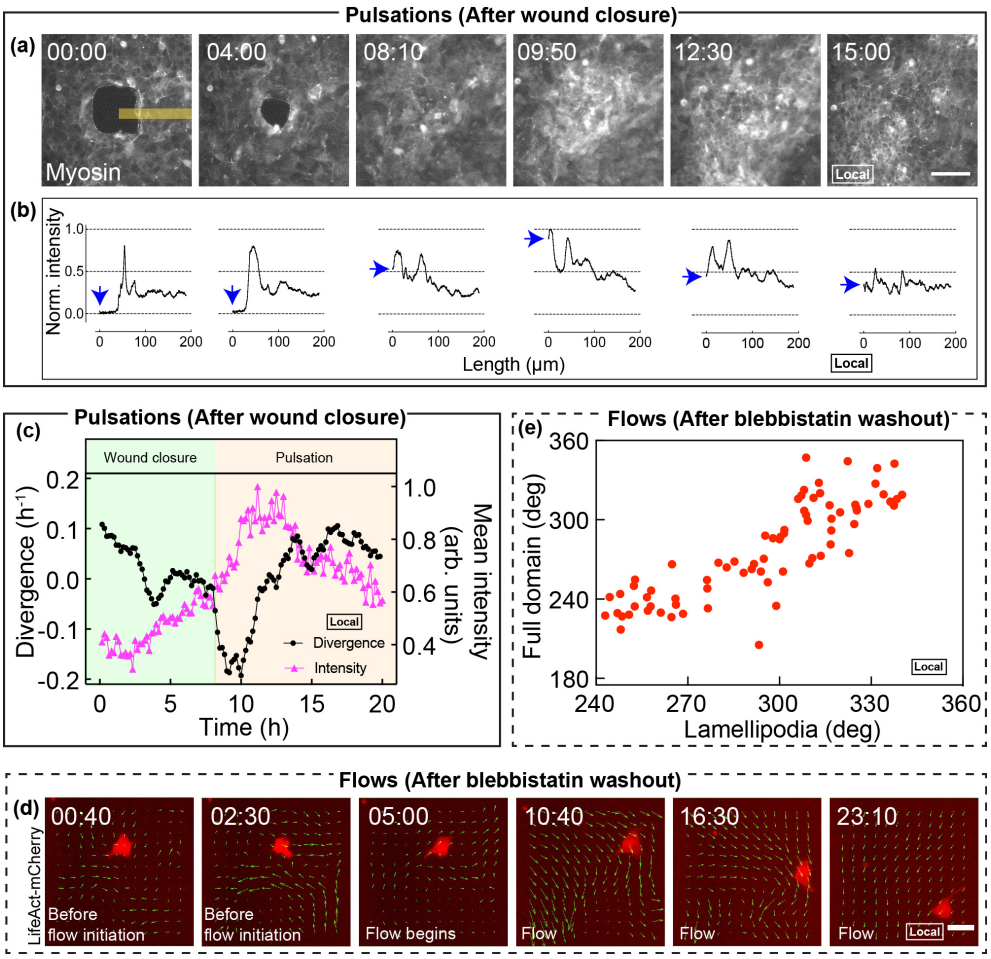

Figure 4. Molecular actors associated with pulsations and flows. (a)-(c) Fluctuation in myosin density during the contraction and expansion phases of pulsation. Micropillar assay was used to create wounds in the monolayer. Following wound closure, pulsations were observed in these sites. (a) Snapshots showing the fluctuation in myosin-GFP intensity. The first and the second time points show the wound and its eventual closure, respectively. Subsequent time points show the densification and diffusion of myosin. Scale bar, 100 μm and time is in hh:mm. (b) shows myosin intensity profiles obtained along the yellow stripe in (a). Myosin intensity is initially zero at the center (0 μm) of the wound (indicated by blue arrows) and increases to the half-way mark during wound closure. However, as the pulsation begins with contraction (at 12:40 in (a)), myosin intensity reaches the maximum and diffuses back to the half-way mark as the domain extends. See the associated Movie 10, Supp. Fig. 7a and Supp. Fig. 7b. (c) Divergence and intensity plots for the pulsatile domain shown in (a). The green region represents the wound closure phase, and the pink region represents the pulsation phase. (d)-(e) Orientation of lamellipodia aligning with the flow direction (on resetting myosin activity through incubation with blebbistatin for 12 h and wash-out). The first two snapshots in (d) represent the timepoint before flow initiation; the transition to flows is shown by the third time point and the subsequent time points show the flow phase. (d) The lamellipodial orientation of a cell transiently transfected with LifeAct-mCherry, shown in red, is superimposed with the direction of flow field vectors (green). Scale bar, 50 μm, and time is in hh:mm. (e) Plot showing the linear tendency between lamellipodia orientation and the mean flow direction of the domain. The lamellipodia direction (obtained from the effective cell direction – see Supplementary Information Section IE) in the x-axis, is obtained for the cell shown in (d). See the associated Movie 11, Supp. Fig. 7c and 7d.

strongly modulated the correlation length of the tissue-level velocity (see Figs.3a and 3b, Supp. Fig. 6a, and Movies 7 and 8). Specifically, upon the addition of blebbistatin (see Section VIII Materials and Methods), tissue motion was significantly reduced (Supp. Fig. 6a). However, about 2 h after subsequent wash-out of blebbistatin led to the appearance of flows with a longer spatial correlation and more persistence over time (Figs. 3a and 3b, Supp. Fig. 6a and Movie 7), as quantified by the velocity correlation functions. The myosin retrieves its activity within minutes after washout but the cell and the monolayer have their own time to integrate activity and cause flows on 100 μm length scale. A similar effect was also observed following the addition and wash-out of latrunculin-A (Supp. Figs. 6b and 6c and Movie 8). We propose that blebbistatin washout promotes *de novo* monolayer collective order which is distinct from cellular arrangement obtained with standard plating protocol in which cells are randomly distributed at the early time points. We suggest that the formation of new cell-cell contacts after washout resets individual cell polarities to

generate long range flow patterns.

We had observed that pulsations in the MDCK monolayer started around the time when the cells were about to be completely confluent by the closure of gaps or 'wounds' in the tissue. Assuming that an empty space can lead to pulsatile motion of cells, we generated a wound using laser ablation after wash-out of the cytoskeletal inhibitor when the tissue exhibited a strongly coherent flow (see Fig. 3c, Supp. Fig. 6d, and Materials and Methods). Interestingly, cells then underwent back and forth motions with contraction and relaxation after ablation, in a way reminiscent of pulsatile flows observed without treatment (Fig. 3d and Movie 9). This observation was further confirmed by the measurement of divergence and its correlation (Fig. 3e). These results indicate that a combination of cytoskeletal remodeling and physical perturbations can toggle collective cell movements between pulsatile and long-range flows.

V. Cellular mechanisms behind pulsatile flows

Following the same idea as laser ablation, where wound closure led to pulsations, we then sought to generate controlled wounds in the tissue to test their effect on the flow properties. Cells were plated on the substrate with microfabricated pillars, which were then removed, generating regularly placed empty spaces in the tissue. We then noticed that cells around the site of wound closure underwent pulsatile flows (Supp. Figs. 7a and 7b, and Movie 10). We took advantage of this set-up to visualize the cellular myosin distribution in cells participating in pulsatile flows (Fig. 4a). We noticed that contracting zones appeared to exhibit an increased density of myosin. We also observed the transient appearance of a radial gradient of myosin fluorescence intensity around the wound, with larger intensity values towards the center of the wound in the contracting phase. This gradient was more homogeneous in the expanding phase (Figs. 4b and 4c and Movie 10). These results suggest that myosin gradients participate in driving pulsatile flows in the tissue.

We also tested whether cell lamellipodia orientation was correlated with tissue flow. To follow lamellipodia dynamics, we used mosaic experiments with cells transiently transfected with Lifeact-mCherry (Figs. 4d, Supp. Fig. 7c, and Movie 11; also see Materials and Methods). Using blebbistatin wash-out to induce large-scale correlated flows, we found that lamellipodia direction indeed correlated with the movement of cells (Fig. 4e, Supp. Fig. 7c and 7d, and Supplementary Information Section IE). We chose to quantify the lamellipodium orientation by tracking and segmenting the outline of cells labelled with Lifeact-mCherry and calculated a nematic order parameter from

the cell contour. We found that the nematic axis associated with cell elongation was then typically aligned with the direction of the flow (Supplementary Information Section IE, Supp. Fig. 2). These observations support that lamellipodia extend along the direction of flows.

In summary, these observations support the idea that pulsatile contraction and expansion are associated with variations in cell myosin intensity and that cells are polarized along the direction of the flow.

VI. Numerical simulations to model tissue pulsatile flows

To identify the origins of the pulsatile collective flow, we ran numerical simulations of the tissue flow based on a vertex model [28]. In our model, cells were assigned a polarity vector that evolved over time according to a local alignment rule and a polarity diffusion. The cells were subjected to a motile force along the polarity axis (Fig. 5a).

In the basic vertex model of the confluent monolayer, the epithelial cells were represented as polygons that were created with vertices (Fig. 5a). Every pair of adjacent vertices was shared by an edge which in turn had a cell on each of its side. The position of the vertices and the connectivity of the cells defined the geometry and topology, respectively, of the tissue. The mechanical properties were assigned to the minimal vertex model via a work function W:

$$W = \sum_{\alpha=1}^{N} \frac{K_\alpha}{2}(A_\alpha - A_\alpha^0)^2 + \sum_{\alpha\beta} \Lambda_{\alpha\beta} l_{\alpha\beta}. \tag{1}$$

The first term of the work function modeled the isotropic mechanical resistance with stiffness K_α from a cell α having actual area A_α to any deviations from its preferred area A_α^0. The second term represented the effective interaction energy between two connected cells α and β that resulted from a combination of cell-cell adhesion energy ($\Lambda_{\alpha\beta}$) and acto-myosin contractility along the shared edge $\alpha\beta$ length $l_{\alpha\beta}$. The force acting on a particular vertex i with position $\mathbf{r}_i$ was

$$\mathbf{F}_{\text{basic}} = -\frac{\partial W}{\partial \mathbf{r}_i}. \tag{2}$$

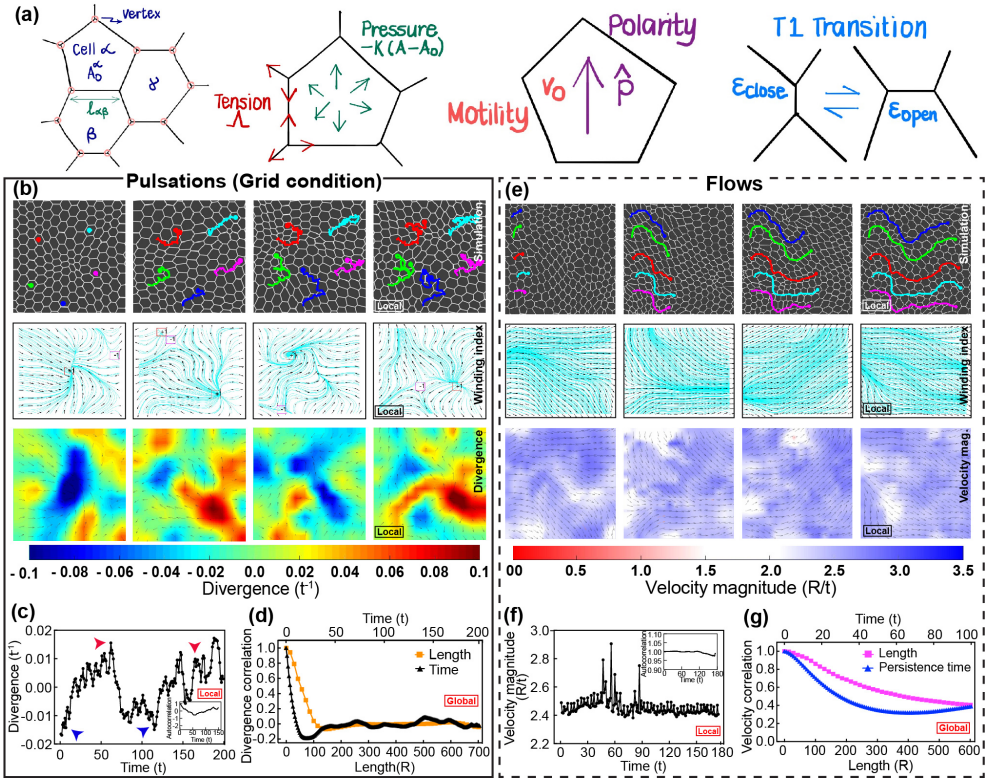

Figure 5. Simulations of pulsations in friction grid and flows using active vertex model. (a) Basic schematic of the vertex model and the source of forces on the vertices. The outcome of simulations for friction grid (b)-(d) and flows (e)-(g) correspond to their experimental counterparts in Figures 2 and 3, respectively. In (b), the first row shows: periodic contraction and expansion of a local domain with the back-and-forth movement of cells. The second and third rows show the topological defects from winding number analysis and divergence, respectively. Color coding: blue indicates contraction and red indicates expansion in the panels showing divergence field. See the associated Movie 13. (c) Total divergence for the local domain shown in (b) as a function of time. The time periodicity is apparent from the corresponding time autocorrelation function shown in the inset. (d) The time and space correlations for divergence over the entire simulation. As observed in the experimental findings, length and time scales emerged from the divergence correlation plots. In (e), the first row shows the presence of long-range flows in the selected region. The second and third rows show the absence of topological defects and velocity magnitude, respectively. Color coding: red and blue indicate low and high velocities in those panels representing velocity magnitude. See the associated Movie 15. (f) The corresponding velocity magnitude within the domain in (e) is nearly constant in time. Inset shows the autocorrelation. (g) Velocity correlation function over the entire simulation shows persistence (long correlation) in both space and time. For a detailed discussion on experimental units of time and length, see Supplementary Information Section ID.

The cells within the colony were polarised and had a tendency to migrate (Fig. 4). The motility behavior of an isolated polarised cell was modeled using a simple description in which the cell moved with speed v_0 along its polarity direction $\hat{\mathbf{p}}$. For the vertex model, this self-propulsion tendency of cells was converted to an effective motile force on its constituent vertex i as

$$\mathbf{F}_{\text{motile}} = \eta v_0 \frac{1}{N_i} \sum_{\text{cell}\beta} \hat{\mathbf{p}}_\beta, \tag{3}$$

where summation was over the polarities $\hat{\mathbf{p}}_\beta$, respectively, of the N_i cells that contain the vertex i, and η is the effective friction coefficient between the cell vertex and the substrate [28, 29].

Initially, $N = 3060$ cells were created in a periodic box of size $L_x \times L_y$. Each cell is provided a polarity $\hat{\mathbf{p}} = \cos\phi \mathbf{e}_x + \cos\phi \mathbf{e}_y$, where the angle ϕ was chosen randomly from $[0, 2\pi)$. The time evolution of vertex positions $\mathbf{r}_i$ was based on the equation

$$\eta \frac{d\mathbf{r}_i}{dt} = \mathbf{F}_{\text{basic}} + \mathbf{F}_{\text{motile}}. \tag{4}$$

To temporally evolve the polarity of the cells we utilised the experimental observations depicted in Supp. Fig. 2. Specifically, we assumed that the polarity vector $\hat{\mathbf{p}}_\alpha$ for a cell α has two tendencies – (i) to align with the direction $\hat{\mathbf{v}}_\alpha$ of its instantaneous velocity and (ii) to undergo rotational diffusion – which mathematically translated to the following differential equation [30, 31]

$$\frac{d\hat{\mathbf{p}}_\alpha}{dt} = (\xi m^\alpha_{\text{align}} + \xi^\alpha_{\text{rand}})\hat{\mathbf{p}}^\perp_\alpha, \tag{5}$$

$$m^\alpha_{\text{align}} = (\hat{\mathbf{p}}_\alpha \times \hat{\mathbf{v}}_\alpha) \cdot \hat{\mathbf{e}}_z \text{ and } \hat{\mathbf{e}}_z = \hat{\mathbf{p}}_\alpha \times \hat{\mathbf{p}}^\perp_\alpha. \tag{6}$$

Here, ξ was the alignment strength of polarity and ξ_{rand} was the diffusive, rotational, Gaussian noise with strength D_r. The differential equations were solved using an explicit forward scheme with a time-step Δt. See Supplementary Information Section ID for additional details. Our model had seven parameters: preferred cell area (A_0), cell area modulus (K_0), line tension of cell interfaces (Λ), cell motility (v_0), polarity alignment rate (ξ), rotational diffusion of polarity (D_r), and substrate friction coefficient (η). From these parameters, a set of time scales can be defined (Supplementary Information Section ID).

We first tested the simulations with periodic boundary conditions and no rotational noise on the cell polarity vector and failed to generate pulsations. However, flows of cells were observed in many of the versions [32]. This finding suggests that the generation of pulsations required another element, provided here by the rotational noise on cell polarity. We found that the absolute and the relative

values of ξ and D_r were important in setting the nature of collective migration modes in the tissue (see Supplementary Information Section ID). High values of ξ promote polarity alignment in some direction, and hence long-range flows. On the contrary, high values of D_r promoted fast and short-range oscillations. When the relative values of D_r and ξ were well-balanced, we found temporally periodic and spatially oscillatory migration patterns of cells similar to that experimentally observed.

We next sought to reproduce three experimental conditions (Fig. 5, Supp. Fig. 8, and Movies 12–15). We numerically mimicked standard monolayer (Supp. Fig. 8a, Movie 12), monolayer on grid (Fig. 5b and Movie 13), and flows after blebbistatin wash-out (Fig. 5e and Movie 15). To perform these numerical experiments, we tested the parameters that could allow reproduction of the experimental data. To be quantitative, we also plotted the divergence correlation and the velocity correlation as a function of time and space. The three situations are represented in Fig. 5d, Fig. 5g, and Supp. Fig. 8c, all of which show good agreement with our data. We needed to have $\frac{\xi}{D_r} \sim 1$, grid-dependent friction, and $\frac{\xi}{D_r} \gg 1$ to produce, respectively, Supp. Figs. 8bc, Figs. 5cd, and Figs. 5fg. Interestingly, we could also mimic the agitated movement of cells observed in a fibronectin grid with a PEG coating at the center, which is expected to reduce cell-substrate friction in that region (Movie 14). We note that it is the differential friction between the central region and the adhesive patch of the simulated grid that leads to the modification in the pattern of cellular movements. Interestingly, the velocity patterns were more pronounced when the difference in the friction between the two regions was greater.

Our model assumptions and predictions are consistent with experimental observations. When the velocity direction and polarity at any position in monolayer were weakly correlated, pulsation was the main mode of cell movements (Supp. Figs. 9a,b and Supplementary Material Section IE). In contrast, when the velocity-polarity correlation was strong, cell flows were dominant (Supp. Figs. 9c,d and Supplementary Information Section IE). In our model, the velocity alignment term ξ tends to align cell polarity with its velocity direction, whereas the rotational noise D_r perturbs this alignment. Taken together, these observations support our modeling results that when velocity alignment strength is dominant ($\xi/D_r \ll 1$), we obtain long range cellular flows. However, when the strength of velocity alignment and random rotation are comparable ($\xi/D_r \sim 1$), we generate pulsatory cell movements.

Taken together, these results reproduce the main observations of our experiments. We conclude

that a simple combination of cell motility and polarity dynamics could account for the pulsatile nature of the flow. More specifically, modulating substrate friction, polarity diffusion and the strength of polarity-velocity alignment led to a variations in tissue kinematics.

VII. Discussion

Pulsations and flows in tissues are striking examples of collective motions. Although pulsations and flows have independently been studied earlier in MDCK monolayers [25, 26, 33–39], in this paper, we generated both types of multi-cellular dynamics in the same epithelial monolayers. We controlled each of them by spatially modulating substrate friction and by introducing in and then washing-out cytoskeletal inhibitors. We revealed that these perturbations affected the external environment and internal cellular properties of the monolayers, leading to these distinct robust collective motions. We also successfully reproduced these dynamics in a minimal vertex model with cell motility that took rotational diffusion of polarity and polarity-velocity alignment as essential components. In this model, a simple change in respective weights of these two polarity mechanisms resulted in a switch between pulsations and long-range flows, showing a way to control collective cell motions in monolayers. Thus, these findings open up a new perspective on using these readouts and numerical simulations to test morphogenetic events in general.

It is interesting to note that the domains for pulsations and flows are about 100 μm in length scales for time scales of about few hours. These similar values can be obtained by scaling arguments. The Maxwell time τ is the ratio of viscosity over Young's modulus. Taking viscosity of about 10^7 Pa.s and Young modulus of about 10^3 Pa [40, 41], we obtain τ of the order of hours. Cell motile speeds are about $v_0 \sim 20$ μm/h. The product $\tau \times v_0$ gives $l \approx 100$ μm. Altogether, these estimates support a simple viscoelastic behavior.

Collective cell migrations *in vivo* occur in an integrated manner, involving signaling and mechanics pathways. For example, in zebrafish, that the so-called lateral line undergoes collective migration through chemical gradients generated by the tissue itself [4, 42]. Similarly, in *Xenopus laevis* neural crest cells, stiffening is involved in setting the mesenchymal to epithelial transition through mechanisms involving an interplay between tissue mechanics and local signalling [43, 44]. Still, mechanical events alone were sufficient to capture some morphogenetic events; therefore, this search for physical rules is essential to capture the deformation kinematics of tissues. For instance, cell motility per se was associated with the elongation of the amniote axis. Similarly, differential

random motion of cells was reported to control somitogenesis in chicken embryos [45–47]. Even if gradients in fibroblast growth factor (FGF) signaling were also present as well in this case, the cellular dynamics were sufficient as the main driving force for elongation, supporting the need to look for physical principles piloting morphogenesis. Germ cells were also shown in many organisms to move towards the gonads through active and passive processes associated with the dynamics of the surrounding tissues [48, 49]. Our generic mechanisms of tissue dynamics for identical cell lines could serve as a framework to revisit these examples guided by the quantification procedure and theoretical methods developed in this study.

In this context, we herein report two types of collective cell motion and provide a generic framework to explain them. Pulsatile movements were observed in various conditions. For example, in *Drosophila*, pulsed contractions guided by acto-myosin are involved in apical constriction and abdominal morphogenesis [11, 50, 51]. Moreover, oscillation may vary across the tissues, as shown in *Drosophila* abdominal morphogenesis [51], and the accompanying myosin gradients are reminiscent of the ones we report in the current study. Elsewhere, oscillations within filopodia during the heart formation of *Drosophila* are essential to optimize morphogenesis in a proof-reading mechanism [52, 53]. Cardiomyocytes also undergo these oscillatory motions both *in vivo* and *in vitro* [54]. This expanding list of pulsation incidences suggests that a self-organized 'pacemaker' associated with a simple pulsation mechanism of physical origin, which span various tissues, model organisms, timescales, and length scales, could be involved in these situations.

We propose the same extension from our study for describing flows *in vivo* [55]. A previous study has shown how forces drive epithelial spreading in zebrafish gastrulation through a flow-friction mechanism [7]. During epiboly in the insect *Tribolium castaneum*, part of the tissue becomes solid and pulls the associated tissues undergoing rearrangement and direct flow [8, 56]. A similar mechanism was suggested during wing formation in *Drosophila* with the hinge and the connected blade [6]. Force balance associated to adhesion between the blastoderm and the vitelline envelope led to this long-range flow. In another context, acto-myosin cables were shown to lead to collective movement of cells in a manner reminiscent to a liquid flow [57]. These situations show similar cell flows to that in the present study. Our study suggests that a common mechanism across scales, tissues, and species may be related to the greater contribution of velocity alignment than rotational diffusion in polarity. Lamellipodia in cells and its actin dynamics could be the main motor in these

long-range flows.

This search for simplicity in the multi-cellular mode aims at extracting generic principles of morphogenesis. The MDCK epithelial monolayer in this study is an excellent system to mimic any epithelial dynamics *in vivo*. As mentioned above, collective cellular motions and deformations are common in developmental biology. However, the focus is generally on the genetic and signaling pathways associated with their onsets. Our *in vitro* results suggest that our readouts of diffusion in polarity and cell alignment can be used *in vivo* to test mechanisms for collective modes during morphogenesis. Because these parameters are now identified, collective cell dynamics can be tested with the same framework across species. Considering the large number of model systems available, including *Drosophila*, *C. elegans*, to zebrafish, *Xenopus*, and mice, these self-organization rules could be explored experimentally and compared across organs and species.

Our current study focused mainly on the physical parameters (substrate friction, cell motility, diffusion in polarity, and polarity-velocity alignment) controlling these types of motion and their cellular readouts through lamellipodia distributions and myosin gradients. In the future, it would be interesting to study the coupling between mechanical processes and cellular signaling, with experimental measurements of both types of events and their inclusions in the associated computational framework [58]. Indeed, recent works have highlighted the connection of wave propagation in tissues with signaling. Mechanical events alter signaling activity and these feedbacks are mediated by mechanochemical interactions between cells through extracellular-signal-regulated kinase (ERK) activation [58]. Investigations on such interplay between mechanical and chemical contractions and waves could generate new paradigms in morphogenesis and allow the identification of conserved principles of mechanics and signaling networks in living matter.

VIII. Materials and Methods

A. Cell culture and cytoskeletal drugs

MDCK cells labelled with Green Fluorescent Protein (GFP) for E-Cadherin (gift from Nelson lab, Stanford University), MDCK cells labelled with actin-mcherry/myosin-GFP (gift from Roland Soldner lab), and MDCK cells labelled with GFP for myosin (gift from Shigenobu Yonemura lab, RIKEN) were cultured at 37°C in low-glucose Dulbecco's modified Eagle's medium (DMEM) (31885-049, Inivtrogen) supplemented with 10% Fetal Bovine Serum (FBS) (10309433, HyClone) and 1% antibiotics (Penicillin-Streptomycin; 11548876, Invitrogen). Cells were maintained at a minimal

confluency of $40\% - 50\%$ and then trypsinized at $70\% - 80\%$ confluency for experiments. Live experiments were performed in Leibovitz L-15 medium (11540556; Invitrogen) and unless mentioned, the initial seeding density was maintained at $\frac{10^6 \text{ cells}}{175\ \mu\text{m}^2}$ for all experiments. For the mosaic experiment, MDCK-Ecadherin-GFP cells transiently transfected with LifeAct-mCherry were mixed with non-transfected cells. To inhibit cytoskeletal proteins, these inhibitors were used at the indicated concentrations: blebbistatin (100 μM) (B0560; Sigma Aldrich) and latrunculin A (1 μM) (L5163, Sigma Aldrich). For each condition, we performed at least three biological repeats.

B. Micro-contact printing

Micropatterning of fibronectin on glass coverslips was performed using the micro-contact printing procedure [59]. First, motifs were microfabricated as SU-8 (MicroChem) molds on silicon wafers using standard photolithography technique. Next, the replica were molded on polydimethylsiloxane (PDMS) (Sylgard 184; Dow Corning) at a pre-polymer, crosslinker ratio – 9 : 1 (V/V)) for micropatterning. During the micro-contact printing procedure, coverslips were hydrophilized with “Piranha" activation [Piranha: 3:7 parts of H_2O_2 (516813; Sigma) and H_2SO_4 (258105; Sigma)] followed by functionalization with (3-mercaptopropyl)trimethoxysilane (S10475, Fluorochem) for 1 h by vapor phase deposition. The coverslips were then dried at 65°C for $\approx$ 2 h. Next, PDMS stamps with microstructures were hydrophilized by oxygen plasma activation (Diener Electronic) and incubated with TRITC or HiLyte 488-labelled Fibronectin (FNR01/FNR02; Cytoskeleton) (10 μg/ml) for 1 h. The dried stamp was then brought in contact with the activated coverslip and a gentle pressure was applied to transfer the fibronectin patterns from the PDMS stamps to the coverslip. The coverslip was then stored in phosphate buffered saline (PBS) (11530486; Invitrogen) solution at 4°C until the time of cell seeding. If the non-printed zones were to be passivated, the micropatterned coverslip was brought in contact with PLL-g-PEG (poly-L-Lysine-grafted-PolyEthylene Glycol) (100 μg/ml) (SuSoS) in 10mM HEPES (pH 7.4) solution for 20 min. Then the coverslips were subsequently rinsed with PBS before proceeding for cell seeding.

C. Wound healing experiments

Wound healing experiments were performed using microfabricated pillars [60]. A PDMS stamp with micropatterns was incubated with 0.2% pluronic acid (P2443, Sigma Aldrich) for 1 h and then rinsed with PBS. The stamp was then activated using an O_2 plasma cleaner and the side with micropillars was brought in contact with an activated glass coverslip for bonding. The bonded stamp

and coverslip were stored at 65°C for 30 min to strengthen the bonding. After UV sterilization of the stamp and coverslip, cells at a concentration of approximately 10^6 cells/20 μl were added at the interface between the stamp and the coverslip. The cells filled the space between the micropillars and they were allowed to settle for 45 min. Once the cells have settled, fresh DMEM media was added to the sample which was then stored at 37°C for $\approx$ 12 h to allow cell spreading between the micropillars. After $\approx$ 12 h, the PDMS stamp was carefully peeled off from the coverslip and the sample was finally rinsed and filled with L-15 media before imaging was started. For more details regarding experiments, analysis, and theory, please see Supplementary Information. The movie captions are also presented in Supplementary Information.

Data and Code Availability

All data generated or analysed in this study are available from the corresponding authors upon reasonable request. Codes to analyse the data and perform numeric calculations are available from the corresponding authors upon reasonable request.

Acknowledgments

We thank Frank Jülicher, S. S. Soumya, and Vikram Gadre for helpful discussions, and Romain Levayer and Julien Vermot for important feedbacks on morphogenesis in developmental biology. We thank the Riveline Lab for discussions and help, and we acknowledge the Imaging Platform from IGBMC. We are grateful to W. James Nelson, Shigenobu Yonemura, Roland Wedlich-Söldner, and Sylvie Coscoy labs for sending cell lines. D.R. acknowledges support from CNRS (ATIP), ciFRC Strasbourg, the University of Strasbourg, Labex IGBMC. This study with the reference ANR-10-LABX-0030-INRT has been also supported by a French state fund through the Agence Nationale de la Recherche under the frame programme Investissements d'Avenir labelled ANR-10-IDEX-0002-02. R.T. was an IGBMC International PhD Programme fellow supported by LabEx INRT funds. M.M.I. acknowledges funding from Department of Biotechnology, Government of India (BT/06/IYBA/2012), Science and Engineering Research Board (MTR/2020/000605), and Industrial Research and Consultancy Center (IRCC), IIT Bombay. G.S. was supported by the Francis Crick Institute which receives its core funding from Cancer Research UK (FC001317), the UK Medical Research Council (FC001317), and the Wellcome Trust (FC001317). D.R. and M.M.I.

also acknowledge hospitality at MPI-PKS, Dresden, where a part of this work was done.

---

[1] Matteo Rauzi, Pierre-François Lenne, and Thomas Lecuit. Planar polarized actomyosin contractile flows control epithelial junction remodelling. *Nature*, 468(7327):1110–1114, December 2010.

[2] Benoît Aigouy, Reza Farhadifar, Douglas B. Staple, Andreas Sagner, Jens-Christian Röper, Frank Jülicher, and Suzanne Eaton. Cell Flow Reorients the Axis of Planar Polarity in the Wing Epithelium of Drosophila. *Cell*, 142(5):773–786, September 2010.

[3] Minna Roh-Johnson, Gidi Shemer, Christopher D. Higgins, Joseph H. McClellan, Adam D. Werts, U. Serdar Tulu, Liang Gao, Eric Betzig, Daniel P. Kiehart, and Bob Goldstein. Triggering a Cell Shape Change by Exploiting Preexisting Actomyosin Contractions. *Science*, 335(6073):1232–1235, March 2012.

[4] Erika Donà, Joseph D. Barry, Guillaume Valentin, Charlotte Quirin, Anton Khmelinskii, Andreas Kunze, Sevi Durdu, Lionel R. Newton, Ana Fernandez-Minan, Wolfgang Huber, Michael Knop, and Darren Gilmour. Directional tissue migration through a self-generated chemokine gradient. *Nature*, 503(7475):285–289, November 2013.

[5] Bing He, Konstantin Doubrovinski, Oleg Polyakov, and Eric Wieschaus. Apical constriction drives tissue-scale hydrodynamic flow to mediate cell elongation. *Nature*, 508(7496):392–396, April 2014.

[6] Raphaël Etournay, Marko Popović, Matthias Merkel, Amitabha Nandi, Corinna Blasse, Benoît Aigouy, Holger Brandl, Gene Myers, Guillaume Salbreux, Frank Jülicher, and Suzanne Eaton. Interplay of cell dynamics and epithelial tension during morphogenesis of the Drosophila pupal wing. *eLife*, 4:e07090, June 2015.

[7] M. Behrndt, G. Salbreux, P. Campinho, R. Hauschild, F. Oswald, J. Roensch, S. W. Grill, and C.-P. Heisenberg. Forces Driving Epithelial Spreading in Zebrafish Gastrulation. *Science*, 338(6104):257–260, October 2012.

[8] Stefan Münster, Akanksha Jain, Alexander Mietke, Anastasios Pavlopoulos, Stephan W. Grill, and Pavel Tomancak. Attachment of the blastoderm to the vitelline envelope affects gastrulation of insects. *Nature*, 568(7752):395–399, April 2019.

[9] Jonathan B. Michaux, François B. Robin, William M. McFadden, and Edwin M. Munro. Excitable RhoA dynamics drive pulsed contractions in the early C. elegans embryo. *Journal of Cell Biology*, 217(12):4230–4252, December 2018.

[10] Huimin Zhang and Michel Labouesse. Signalling through mechanical inputs – a coordinated process. *Journal of Cell Science*, 125(13):3039–3049, July 2012.

[11] Adam C. Martin, Matthias Kaschube, and Eric F. Wieschaus. Pulsed contractions of an actin–myosin network drive apical constriction. *Nature*, 457(7228):495–499, January 2009.

[12] Xavier Trepat and Erik Sahai. Mesoscale physical principles of collective cell organization. *Nature Physics*, 14(7):671–682, July 2018.

[13] B. Geiger, S. Yehuda-Levenberg, and A. D. Bershadsky. Molecular Interactions in the Submembrane Plaque of Cell-Cell and Cell-Matrix Adhesions. *Cells Tissues Organs*, 154(1):46–62, 1995.

[14] François Graner and Daniel Riveline. 'The Forms of Tissues, or Cell-aggregates': D'Arcy Thompson's influence and its limits. *Development*, 144(23):4226–4237, December 2017.

[15] I. Geudens and H. Gerhardt. Coordinating cell behaviour during blood vessel formation. *Development*, 138(21):4569–4583, November 2011.

[16] Charles Betz, Anna Lenard, Heinz-Georg Belting, and Markus Affolter. Cell behaviors and dynamics during angiogenesis. *Development*, 143(13):2249–2260, July 2016.

[17] Markus Affolter, Rolf Zeller, and Emmanuel Caussinus. Tissue remodelling through branching morphogenesis. *Nature Reviews Molecular Cell Biology*, 10(12):831–842, December 2009.

[18] A. Ochoa-Espinosa and M. Affolter. Branching Morphogenesis: From Cells to Organs and Back. *Cold Spring Harbor Perspectives in Biology*, 4(10):a008243–a008243, October 2012.

[19] Buzz Baum and Marios Georgiou. Dynamics of adherens junctions in epithelial establishment, maintenance, and remodeling. *The Journal of Cell Biology*, 192(6):907–917, March 2011.

[20] Sham Tlili, Estelle Gauquelin, Brigitte Li, Olivier Cardoso, Benoît Ladoux, Hélène Delanoë-Ayari, and François Graner. Collective cell migration without proliferation: Density determines cell velocity and wave velocity. *Royal Society Open Science*, 5(5):172421.

[21] M. Reza Shaebani, Adam Wysocki, Roland G. Winkler, Gerhard Gompper, and Heiko Rieger. Computational models for active matter. *Nature Reviews Physics*, 2(4):181–199, April 2020.

[22] Jerome Irianto, Charlotte R. Pfeifer, Yuntao Xia, and Dennis E. Discher. SnapShot: Mechanosensing Matrix. *Cell*, 165(7):1820–1820.e1, June 2016.

[23] Raghu Kalluri and Robert A. Weinberg. The basics of epithelial-mesenchymal transition. *The Journal of Clinical Investigation*, 119(6):1420–1428, June 2009.

[24] Olivia du Roure, Alexandre Saez, Axel Buguin, Robert H. Austin, Philippe Chavrier, Pascal Siberzan, and Benoit Ladoux. Force mapping in epithelial cell migration. *Proceedings of the National Academy of Sciences*, 102(7):2390–2395, February 2005.

[25] Thomas E. Angelini, Edouard Hannezo, Xavier Trepat, Jeffrey J. Fredberg, and David A. Weitz. Cell Migration Driven by Cooperative Substrate Deformation Patterns. *Physical Review Letters*, 104(16):168104, April 2010.

[26] M. Poujade, E. Grasland-Mongrain, A. Hertzog, J. Jouanneau, P. Chavrier, B. Ladoux, A. Buguin, and P. Silberzan. Collective migration of an epithelial monolayer in response to a model wound. *Proceedings of the National Academy of Sciences*, 104(41):15988–15993, October 2007.

[27] S. Tlili, M. Durande, C. Gay, B. Ladoux, F. Graner, and H. Delanoë-Ayari. Migrating Epithelial Monolayer Flows Like a Maxwell Viscoelastic Liquid. *Physical Review Letters*, 125(8):088102, August 2020.

[28] Jordi Comelles, Soumya S S, Linjie Lu, Emilie Le-Maout, Sudakar Anvitha, Guillaume Salbreux, Frank Jülicher, Mandar M Inamdar, and Daniel Riveline. Epithelial colonies in vitro elongate through collective effects. *eLife*, 10:e57730, January 2021.

[29] Daniel M. Sussman. cellGPU: Massively parallel simulations of dynamic vertex models. *Computer Physics Communications*, 219:400–406, October 2017.

[30] Silke Henkes, Yaouen Fily, and M. Cristina Marchetti. Active jamming: Self-propelled soft particles at high density. *Physical Review E*, 84(4):040301, October 2011.

[31] S. S. Soumya, Animesh Gupta, Andrea Cugno, Luca Deseri, Kaushik Dayal, Dibyendu Das, Shamik Sen, and Mandar M. Inamdar. Coherent Motion of Monolayer Sheets under Confinement and Its Pathological Implications. *PLOS Computational Biology*, 11(12):e1004670, December 2015.

[32] M. C. Marchetti, J. F. Joanny, S. Ramaswamy, T. B. Liverpool, J. Prost, Madan Rao, and R. Aditi Simha. Hydrodynamics of soft active matter. *Reviews of Modern Physics*, 85(3):1143–1189, July 2013.

[33] L. Petitjean, M. Reffay, E. Grasland-Mongrain, M. Poujade, B. Ladoux, A. Buguin, and P. Silberzan. Velocity Fields in a Collectively Migrating Epithelium. *Biophysical Journal*, 98(9):1790–1800, May 2010.

[34] Steven M. Zehnder, Federico M. Zegers, and Thomas E. Angelini. A Langevin model of physical forces in cell volume fluctuations. *Journal of Biomechanics*, 49(8):1286–1289, May 2016.

[35] Steven M. Zehnder, Melanie Suaris, Madisonclaire M. Bellaire, and Thomas E. Angelini. Cell Volume Fluctuations in MDCK Monolayers. *Biophysical Journal*, 108(2):247–250, January 2015.

[36] Grégoire Peyret, Romain Mueller, Joseph d'Alessandro, Simon Begnaud, Philippe Marcq, René-Marc Mège, Julia M. Yeomans, Amin Doostmohammadi, and Benoît Ladoux. Sustained Oscillations of Epithelial Cell Sheets. *Biophysical Journal*, 117(3):464–478, August 2019.

[37] Jacob Notbohm, Shiladitya Banerjee, Kazage J. C. Utuje, Bomi Gweon, Hwanseok Jang, Yongdoo Park, Jennifer Shin, James P. Butler, Jeffrey J. Fredberg, and M. Cristina Marchetti. Cellular Contraction and Polarization Drive Collective Cellular Motion. *Biophysical Journal*, 110(12):2729–2738, June 2016.

[38] Pilar Rodríguez-Franco, Agustí Brugués, Ariadna Marín-Llauradó, Vito Conte, Guiomar Solanas, Eduard Batlle, Jeffrey J. Fredberg, Pere Roca-Cusachs, Raimon Sunyer, and Xavier Trepat. Long-lived force patterns and deformation waves at repulsive epithelial boundaries. *Nature Materials*, 16(10):1029–1037, October 2017.

[39] Vanni Petrolli, Magali Le Goff, Monika Tadrous, Kirsten Martens, Cédric Allier, Ondrej Mandula, Lionel Hervé, Silke Henkes, Rastko Sknepnek, Thomas Boudou, Giovanni Cappello, and Martial Balland.

Confinement-Induced Transition between Wavelike Collective Cell Migration Modes. *Physical Review Letters*, 122(16):168101, April 2019.

[40] Karine Guevorkian, Marie-Josée Colbert, Mélanie Durth, Sylvie Dufour, and Françoise Brochard-Wyart. Aspiration of biological viscoelastic drops. *Physical review letters*, 104(21):218101, 2010.

[41] Tomita Vasilica Stirbat, Abbas Mgharbel, Selena Bodennec, Karine Ferri, Hichem C Mertani, Jean-Paul Rieu, and Hélène Delanoë-Ayari. Fine tuning of tissues' viscosity and surface tension through contractility suggests a new role for α-catenin. *PloS one*, 8(2):e52554, 2013.

[42] V. Lecaudey, G. Cakan-Akdogan, W. H. J. Norton, and D. Gilmour. Dynamic Fgf signaling couples morphogenesis and migration in the zebrafish lateral line primordium. *Development*, 135(16):2695–2705, July 2008.

[43] Elias H. Barriga, Kristian Franze, Guillaume Charras, and Roberto Mayor. Tissue stiffening coordinates morphogenesis by triggering collective cell migration in vivo. *Nature*, 554(7693):523–527, February 2018.

[44] Elena Scarpa and Roberto Mayor. Collective cell migration in development. *Journal of Cell Biology*, 212(2):143–155, January 2016.

[45] Bertrand Bénazéraf, Paul Francois, Ruth E. Baker, Nicolas Denans, Charles D. Little, and Olivier Pourquié. A random cell motility gradient downstream of FGF controls elongation of an amniote embryo. *Nature*, 466(7303):248–252, July 2010.

[46] Fengzhu Xiong, Wenzhe Ma, Bertrand Bénazéraf, L. Mahadevan, and Olivier Pourquié. Mechanical Coupling Coordinates the Co-elongation of Axial and Paraxial Tissues in Avian Embryos. *Developmental Cell*, 55(3):354–366.e5, November 2020.

[47] Bertrand Bénazéraf, Mathias Beaupeux, Martin Tchernookov, Allison Wallingford, Tasha Salisbury, Amelia Shirtz, Andrew Shirtz, David Huss, Olivier Pourquié, Paul François, and Rusty Lansford. Multi-scale quantification of tissue behavior during amniote embryo axis elongation. *Development*, 144(23):4462–4472, December 2017.

[48] Azadeh Paksa and Erez Raz. Zebrafish germ cells: Motility and guided migration. *Current Opinion in Cell Biology*, 36:80–85, October 2015.

[49] Cecilia Grimaldi and Erez Raz. Germ cell migration—Evolutionary issues and current understanding. *Seminars in Cell & Developmental Biology*, 100:152–159, April 2020.

[50] Jerome Solon, Aynur Kaya-Çopur, Julien Colombelli, and Damian Brunner. Pulsed Forces Timed by a Ratchet-like Mechanism Drive Directed Tissue Movement during Dorsal Closure. *Cell*, 137(7):1331–1342, June 2009.

[51] Pau Pulido Companys, Anneliese Norris, and Marcus Bischoff. Coordination of cytoskeletal dynamics and cell behaviour during *Drosophila* abdominal morphogenesis. *Journal of Cell Science*, 133(6):jcs235325, March 2020.

[52] Shaobo Zhang, Christopher Amourda, David Garfield, and Timothy E. Saunders. Selective Filopodia Adhesion Ensures Robust Cell Matching in the Drosophila Heart. *Developmental Cell*, 46(2):189–203.e4, July 2018.

[53] Shaobo Zhang, Xiang Teng, Yusuke Toyama, and Timothy E. Saunders. Periodic Oscillations of Myosin-II Mechanically Proofread Cell-Cell Connections to Ensure Robust Formation of the Cardiac Vessel. *Current Biology*, 30(17):3364–3377.e4, September 2020.

[54] Ido Nitsan, Stavit Drori, Yair E. Lewis, Shlomi Cohen, and Shelly Tzlil. Mechanical communication in cardiac cell synchronized beating. *Nature Physics*, 12(5):472–477, May 2016.

[55] Mamoru Ishii, Tomoko Tateya, Michiyuki Matsuda, and Tsuyoshi Hirashima. Interplay between medial nuclear stalling and lateral cellular flow underlies cochlear duct spiral morphogenesis. Preprint, Developmental Biology, July 2020.

[56] Akanksha Jain, Vladimir Ulman, Arghyadip Mukherjee, Mangal Prakash, Marina B. Cuenca, Lokesh G. Pimpale, Stefan Münster, Robert Haase, Kristen A. Panfilio, Florian Jug, Stephan W. Grill, Pavel Tomancak, and Anastasios Pavlopoulos. Regionalized tissue fluidization is required for epithelial gap closure during insect gastrulation. *Nature Communications*, 11(1):5604, December 2020.

[57] Mehdi Saadaoui, Didier Rocancourt, Julian Roussel, Francis Corson, and Jerome Gros. A tensile ring drives tissue flows to shape the gastrulating amniote embryo. *Science*, 367(6476):453–458, January 2020.

[58] Naoya Hino, Leone Rossetti, Ariadna Marín-Llauradó, Kazuhiro Aoki, Xavier Trepat, Michiyuki Matsuda, and Tsuyoshi Hirashima. ERK-Mediated Mechanochemical Waves Direct Collective Cell Polarization. *Developmental Cell*, 53(6):646–660.e8, June 2020.

[59] David Caballero, Raphaël Voituriez, and Daniel Riveline. Protrusion Fluctuations Direct Cell Motion. *Biophysical Journal*, 107(1):34–42, July 2014.

[60] Ester Anon, Xavier Serra-Picamal, Pascal Hersen, Nils C. Gauthier, Michael P. Sheetz, Xavier Trepat, and Benoît Ladoux. Cell crawling mediates collective cell migration to close undamaged epithelial gaps. *Proceedings of the National Academy of Sciences*, 109(27):10891–10896, July 2012.